Spin transport across oxide semiconductors and antiferromagnetic oxide interfaces

Das, Arijit

DOI:
10.33612/diss.150692255

Chapter 5

$SrMnO_3$: a nominal antiferromagnet as revealed by magnetotransport studies

The main part of this chapter is written as a manuscript and is under review: A. Das, V. Eswara Phanindra, A.J. Watson, and T. Banerjee, "Competing magnetic ordering in thin films of $SrMnO_3$ studied by spin transport,"

The ability to tune magnetic ordering in complex oxide based correlated antiferromagnetic insulators, due to the coupling between the charge, spin, lattice and orbital degrees of freedom, opens a vast playground in spintronics. Here we study a tensile strain induced coexistence of a wide range of magnetic ordering in thin films of $SrMnO_3$, as established from the temperature dependence of the spin Hall magnetoresistance (SMR) and spin Seebeck effect (SSE) studies and complemented by structural and bulk magnetization measurements. The temperature dependence of the SMR, SSE and bulk magnetization studies fingerprints the competition between different magnetic domains across the manganite film thickness. Our work demonstrates that strain induced spatial variation of magnetization in such nominal antiferromagnetic manganites can be tuned by orbital ordering and opens new opportunities in antiferromagnetic spintronics.

5.1 Introduction

Identifying and controlling the antiferromagnetic order parameter via Neel vector manipulation and its electrical detection is actively researched in different antiferromagnets [1–3]. Charge-spin or spin-charge conversion methods such as the (Inverse) Spin Hall effects are commonly used to probe key parameters associated with the antiferromagnetic ordering [4–6]. Spin hall magnetoresistance (SMR) and spin Seebeck techniques have evolved in recent years as efficient magnetic probes for studying a wide range of magnetic systems such as ferro/ferrimagnets[7–10], antiferromagnets[4, 5, 11, 12] and frustated systems including paramagnets [13]. However, in this context strongly correlated rare earth manganites exhibiting rich magnetic phase diagram [14, 15] has remained largely unexplored but is an important platform for the design and tunability of diverse magnetic phases and for developing antiferromagnetic oxide based spintronics.

$SrMnO_3$ (SMO) is one of the end members of the $La_{1-x}Sr_xMnO_3$ family. In bulk, it exhibits three different polymorph phases namely; cubic, 4H and 6H hexagonal phases, stabilized at different growth temperatures [16].

All the polymorphs exhibit fully compensated G-type antiferromagnetic-insulating behavior with Neel temperature (T_N) varying between 260 - 278 K [16, 17]. The antiferromagnetic exchange in bulk SMO is governed by the superexchange interaction between the Mn^{4+} ions that preserve the degeneracy of the e_g orbitals of Mn^{4+}. Thin films of SMO, on the other hand, can be tailored to exhibit a wide range of magnetic ordering. For example, by tuning epitaxial strain, the antiferromagnetic (AFM) ordering in thin SMO films can be tuned from G-type to C/A-type[18, 19]. In addition, controlled tuning of different growth conditions can also lead to coexistence of different magnetically ordered phases for this end member of the manganite family. Typical among them being a ferromagnetic insulating phase brought about by the structural distortion of the oxygen octahedra and leading to oxygen deficient $SrMnO_{3-\delta}$ phase [20]. Moreover, first principle calculations have predicted that tensile or compressive strain can drive a series of magnetic phase transitions that couples with the ferroelectric order in SMO and were corroborated by experimental studies [19, 21–24]. Integrating SMO in bilayers with members within the same manganite family, has shown to result in unconventional magnetic features such as a spin glass state and ferromagnetic ordering induced by orbital reconstruction at the interface [25, 26]. In spite of this, an understanding of the strength and nature of magnetic ordering in nominally antiferromagnetic thin films of SMO is sparse and remains a challenge, given the multitude of magnetic phases that can coexist even when adopting careful growth strategies. In this work, we show the richness of the coexisting magnetically ordered states that can be induced in SMO thin films by tuning the deposition parameters and probed by complementary bulk and surface magnetization techniques, with the aim to use this material for AFM based oxide spintronics.

5.2 SMO thin films - related oxygen deficient structures

As discussed above SMO is known to exist in different oxygen deficient states, hence SMO is often represented as $SrMnO_{3-\delta}$. Among the differ-

ent non-stoichiometric $SrMnO_{3-\delta}$ phases, $\delta = 0.5$ is a commonly observed crystalline structure of SMO, i.e $SrMnO_{2.5}$. This phase is known as the brownmillerite-SMO (B-SMO). The space group of B-SMO is Pbam. Interestingly, due to electron doping, B-SMO promotes orbital ordering of Mn^{3+}. In this phase, SMO orders antiferromagnetically with Mn^{3+} ions with Mx (x-direction) =0.5 and My (y-direction) = 2.5 μ_B. The neutron diffraction study in B-SMO indicates an antiferromagnetic alignment with magnetic moments pointing towards the b-axis and both antiferromagnetic and ferromagnetic alignment out-of-plane (c-axis)[27].
This section, gives an overview of the different crystallographic phases that coexist in the thin films of SMO. The films are grown either by molecular epitaxy (MBE) or by pulsed laser deposition (PLD) on different substrates like $SrTiO_3$ (STO) with c-axis in different directions, $LaAlO_3$ (LAO) and LSAT[18]. During thin film growth using PLD, parameters like the oxygen pressure, temperature of the substrate, laser fluence are found to influence the crystalline quality of thin films. Laser fluence is known to affect the Sr/Mn ratio in the SMO thin films[28]. This can give rise to different non-stoichiometric growth of SMO. Moreover, higher temperature of the substrate is known to improve the crystalline quality of the thin films. The Cubic form of SMO (C-SMO), has been found to grow at a very high temperature ($\geq 1000^oC$) on STO (001). In the perovskite $SrMnO_3$ film, the formation of oxygen vacancies is generally charge-compensated by a reduction of the oxidation state of Mn^{4+} to Mn^{3+} possibly resulting in ferromagnetic behavior due to the double exchange. The tensile strain from the substrate promotes oxygen deficient SMO growth leading to $SrMnO_{3-\delta}$. In this section, the different stoichiometric phases of SMO thin films achieved by different growth conditions and the associated magnetic orderings are discussed below.

5.2.1 Brownmillerite $SrMnO_{2.5}$ (B-SMO)

Brownmillerite phases of the perovskite films ($ABO_{3-\delta}$) are widely investigated for $SrMnO_{3-\delta}$, $SrCoO_{3-\delta}$ etc. Unlike C-SMO, B-SMO can be ob-

tained by heating STO (001) substrate at temperatures ranging from 700^o C - 800^o C by PLD growth [20]. Using an oxygen pressure ≤ 0.1 mbar, orthorhombic structure of SMO which is found to be stable for Brownmillerite phases are obtained. As already discussed in the earlier section about the bulk B-SMO, thin film B-SMO are also reported to have antiferromagnetic ordering of the Mn^{3+} ions with a Neel transition above room temperature ($T_N = 375$ K).

5.2.2 Perovskite $SrMnO_{3-\delta}$ (P-SMO)

Perovskite phases with oxygen deficient non-stoichiometric SMO thin films can be achieved with PLD. Usually by post-annealing under non-ambient conditions results in oxygen deficient perovskite SMO. Due to double exchange between Mn^{3+} and Mn^{4+} ions, P-SMO exhibits ferromagnetic behavior with a Curie temperature of 75 K[20].

5.2.3 Mixed $SrMnO_{3-\delta}$ (M-SMO)

Mixed phase of SMO in certain conditions are found to co-exist in the SMO films. The perovskite phase develops on the top layer (ferromagnetic) and brownmillerite phase develops on the bottom layer (antiferromagnetic) of the SMO films. As a result it is reported to show an exchange bias in a single film of SMO[20].

5.2.4 Cubic $SrMnO_3$ (C-SMO)

The stoichiometric $SrMnO_3$ thin films possess a cubic structure due to the epitaxial strain from the underlying substrate. The films are found to host tunable anti-ferromagnetic ordering from an A-type to a G-type depending on the percent of strain (also tensile or compressive) from the substrate[18]. Apparently, G/C -type AFM ordering are fully compensated and do not show any exchange bias with a ferromagnetic film in case of a heterostructure. However, reports show a large exchange bias at the interface of LSMO/SMO that results due to the uncompensated spin structure at the interface leading to a spin glass (SG) state[25]. This spin glass state

arises from the competition of the AFM superexchange between Mn^{4+} ions in SMO and the double exchange mechanism between Mn^{4+} - Mn^{3+} ions in LSMO. Often, this competition between the two different magnetic interaction give rise to a tilting of the oxygen octahedra driving a DM interaction that hosts different magnetic topological features at the interface of a bilayer system which will be discussed in details in Chapter 6.
In this work, the temperature dependence of magnetic phases that coexist in thin films of $SrMnO_3$ (SMO) are studied using complementary techniques, (i) bulk magnetization studies using Superconducting Quantum interference device (SQUID), (ii) Surface sensitive SMR response, (iii) bulk sensitive SSE response. Thin films of SMO deposited by adopting different growth strategies and of varying thickness are studied in this work. The different approaches allow for the study of the correlated interplay between tensile strain and oxygen vacancies across $SrMnO_3/SrTiO_3$ interfaces. This work demonstrates the inevitability of coexisting magnetically ordered states, intrinsic to such tensile strained SMO thin films, that are nominally antiferromagnetic, inspite of adopting careful growth strategies, as revealed by spin transport studies.

5.3 Pulsed laser deposition (PLD) of $SrMnO_3$ thin films

Thin films of SMO are grown using the Pulsed laser deposition technique. The substrates (i.e. $SrTiO_3$) undergoes surface treatment and annealing as mentioned in Chapter 3, and were silver pasted in the PLD resistive heater and was loaded in the PLD chamber. Ceramic target of SMO was loaded in the target carousel inside the chamber. The heater was aligned with respect to the RHEED gun in such a way that it points in the normal direction to the target at a distance of 42 mm. The base pressure of the PLD chamber was maintained at 5-7 x 10^{-6} mbar before the substrate was heated and an oxygen flow was permitted inside the chamber. The heater was set to 900^o C, where the substrate that was attached to the heater at a temperature which is 50 to 100^o C lower than the heater temperature. This temper-

ature difference between the substrate and the heater depends largely on the thermal conductivity of different substrates. STO is known to have a higher thermal conductivity than LAO, hence the difference between STO and heater is around 30^o C whereas for LAO the difference goes to about 100^o C. The ideal condition for the growth of cubic SMO was above 1000^o C which was not possible using a resistive heater. The maximum temperature was 900^o C for the deposition. An oxygen pressure of 0.01 mbar to 0.2 mbar have been used for different samples in order to ascertain the quality of the growth of SMO. In all earlier reports regarding the growth of SMO films, three parameters are always crucial, (a) Temperature: In general, increased temperature improves the crystalline quality of the thin films. In our case, the temperature had to be restricted to 900^o C, owing to the maximum achievable temperature for a resistive heater, (b) Oxygen pressure : Optimal oxygen flow is crucial to preserve the stoichiometry, else the films would grow with an oxygen deficient stoichiometry ($SrMnO_{3-\delta}$). Since, the temperature of the film growth is kept constant at 900^o C, different SMO thin films were grown by changing the oxygen pressure. (c) Laser fluence : The stoichiometric content between Sr and Mn, i.e. Sr/Mn ratio can be affected by the non-optimal usage of the laser fluence. Earlier report of Kobayashi et al., has shown a presence of an additional SrO plane in the $SrMnO_{3-\delta}$ films due excess Sr in the Sr/Mn ratio. This ratio can be tuned by increasing the laser fluence. For our deposition, a fluence of 1 J/cm^2 is used which is in the regime for an optimal Sr/Mn ratio as inspired from the works of Kobayashi[28] and Maurel.[18] Larger fluence can induce degradation of the films.

The atomic force microscopy (AFM) images of the grown films are shown in Fig. 5.2. The figure shows the AFM images of the 3 different SMO thin films grown on STO (001). (a) S1: Sample 1, was grown with an oxygen pressure of 0.01 mbar and post annealed at 100 mbar oxygen pressure while cooling down from 900^o C to room temperature at a rate of 5^o C/min. The total number of laser pulses was 950 at a 1Hz repetition rate. (b) S2: Sample 2, was grown with the oxygen pressure same as (a), but was post annealed at an oxygen pressure of 0.006 mbar oxygen pressure while cooling down from 900^o C to room temperature. (c) S3: Sample 3, was

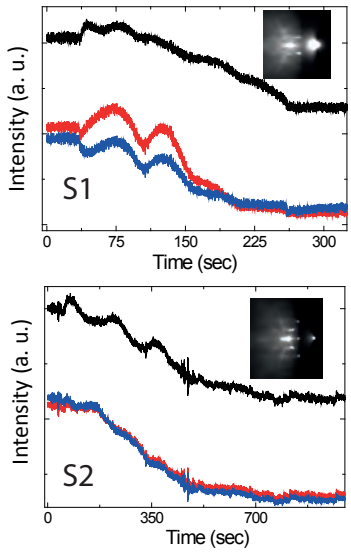

Figure 5.1: RHEED intensity and oscillations for sample S1 (SMO 2 nm / STO), and S2 (SMO 5 nm)/ STO). The unusual increase in the intensity pattern with initial increase in the laser pulses might originate due to the gradual increase in the mixed termination of starting STO substrate due to deposition of $SrMnO_3$ and partial coverage of the SrO sublattices, however this could not be determined due to the lack of microscopic and spectroscopic measurements.

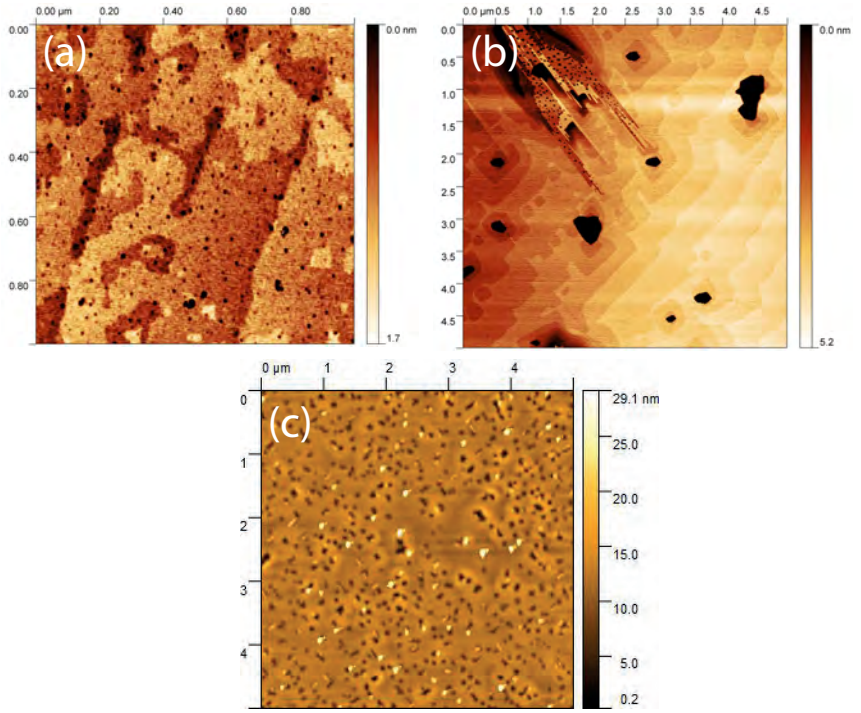

Figure 5.2: AFM images of sample S1 (SMO 2 nm / STO), sample S2 (SMO 5 nm/ STO) and sample S3 (SMO 17 nm/ STO).

grown with an oxygen pressure of 0.2 mbar and post annealed at 100 mbar oxygen pressure. Later, an additional annealing step followed ex-situ at 1 atm pressure for an hour at 900^oC. These different annealing steps resulted in the changing surface topography of SMO films, that were captured in the AFM images. Without any additional annealing step, sample S1 shows clear terraces whereas, in sample S2, the step flow growth was accompanied by island-like growth shown in darker contrast in Fig. 5.2(b). These islands can result due to MnO rich phase that might appear due to lack of oxygen pressure during post-annealing. Sample S3, on the other hand, have been subjected to a more strong annealing process in presence of an oxygen atmosphere. Moreover, the additional annealing step resulted in increasing surface roughness in the S3 film. The RHEED intensity oscillations captured for sample S1 and S2 are shown in Fig. 5.1. Contradicting intensity oscillations were observed prominently for sample S1, where the intensity first increases with the firing of laser pulses, rather than decreasing. With the firing of each pulse, the surface roughness of the substrate increases resulting in a decrease in the RHEED intensity. The reason for increasing intensity with pulses may originate from a starting STO substrate with a mixed termination, which eventually gains a mixed termination due to the coverage of the SrO sublattices from $SrMnO_3$. However, no evidence of such a termination issue could be determined due to the lack of microscopic and spectroscopic measurements. Moreover, the intensity oscillations rather damp quickly resulting in a more island-like growth and increasing surface roughness that are evident in the AFM images. Hence, non-optimal conditions for growth are inferred at such high temperatures.

After the growth, the films were subjected to a 4-probe resistance check at room temperature using an in-house probe station. Sample S2 (5 MΩ) was more conductive than sample S1 (800 MΩ) and sample S3 (1.2 GΩ). Hence sample S2 was not fabricated for spin transport as its conductivity was not suitable for local/non-local spin transport. Samples S1 and S3 have been fabricated for spin transport and hence used for further investigations in this chapter.

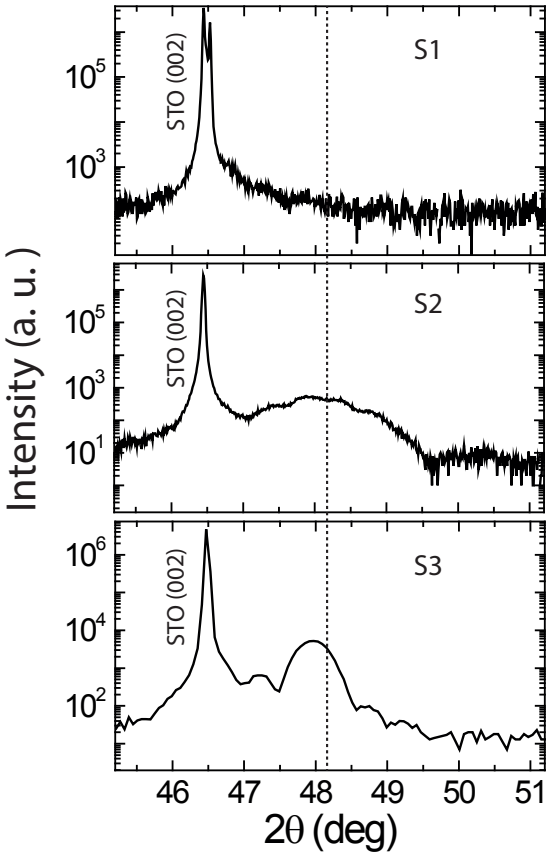

Figure 5.3: XRD ($2\theta - \omega$ plots of sample S1 (SMO 2 nm/ STO), sample S2 (SMO 5 nm/ STO) and sample S3 (SMO 17nm/STO).

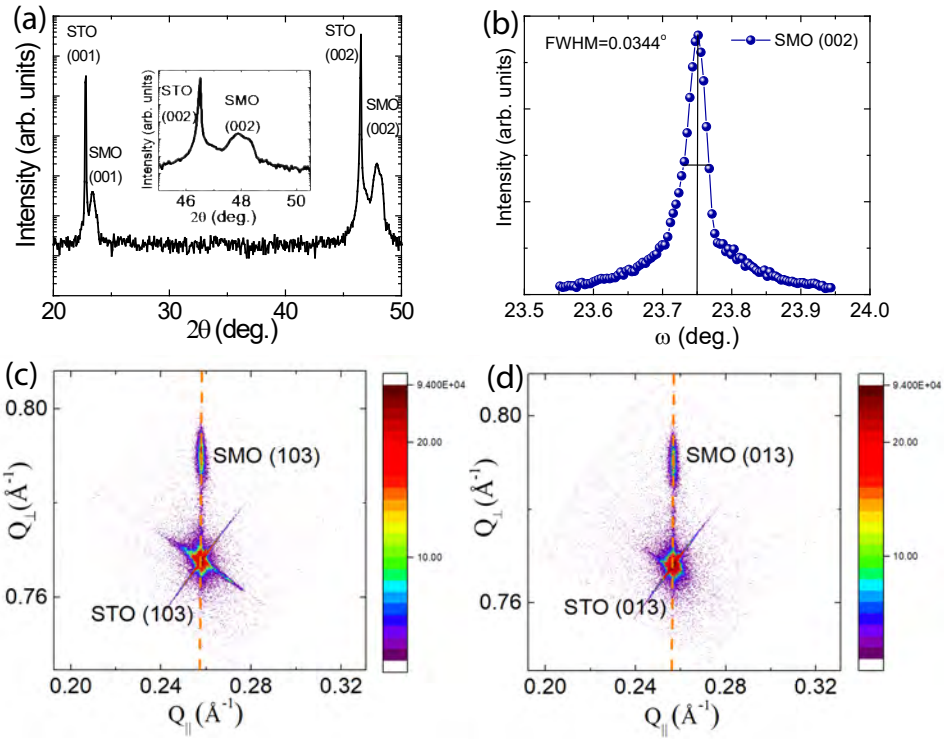

Figure 5.4: (a) XRD θ-2θ scan of epitaxial S3 thin film (broadening of (002) peak as shown in the inset may be due to presence of secondary phases in SMO). Similarly, (b) shows the rocking curve measured along (002) peak of S3 film (FWHM values are obtained from Gaussian fits to experimental data). Reciprocal space maps obtained along (c) (103) and (d) (013) asymmetric reflections depicts the coherent growth (a_{ip} = b_{ip}= 3.905 $\AA$) with both the SMO and STO reflections lying on same pseudomorphic line for the S3 film.

5.4 Structural characterization of $SrMnO_3$ (SMO) thin films

Structural characteristics of the grown SMO films were performed on a PANalytical x-ray diffractometer equipped with a four-axis cradle (Cu k_α radiation, wavelength 1.54 Å). The thickness of the SMO thin films were characterized by X-ray reflectometry and found to be 2 nm and 17 nm for samples S1 and S3 respectively. As can be seen from Fig. 5.3, the sample S1 show no characteristic film peak, the structural characterization were performed for sample S3. The findings of the θ-2θ scans and rocking curves (ω scans) for sample S3 are shown in Fig. 5.4(a and b) and indicate the phase purity and epitaxial relationship of the film with the underlying (001)-oriented STO substrate. Fig. 5.4(c and d) shows the reciprocal space maps (RSM) along (103) and (013) asymmetric peak reflections for the sample S3. It can be seen from the RSM scans that the (013) and (103) asymmetric reflections of both SMO and STO fall on the same pseudomorphic line, suggesting the coherently strained nature of the S3 film with tensile strain/lattice mismatch of $[(a_{film} - a_{bulk})/a_{bulk}] \times 100 = 3.0$ % [29]. Here a_{film}= 3.90 Åand a_{bulk} = 3.79 Åcorresponds to SMO thin film and bulk lattice parameters respectively. Further the RSM maps imply tetragonal symmetry, devoid of any additional crystallographic symmetries of the S3 film with identical in-plane orthogonal lattice parameters ($a_{ip} = b_{ip}$) and compressed out-of-plane lattice constant due to tensile strain induced by the underlying (001)-oriented STO substrate.

5.5 Magnetization studies

Temperature and field-dependent magnetization studies of both SMO films were done using SQUID magnetometer (Quantum Design). Fig. 5.5(a) shows the temperature dependent in-plane hysteresis loops recorded in both zero-field cooled and field cooled modes (H_{FC}= 70 kOe with running field of 500 Oe) for sample S1, after subtracting the linear diamagnetic contribution arising from the STO substrates. The saturation magnetization values

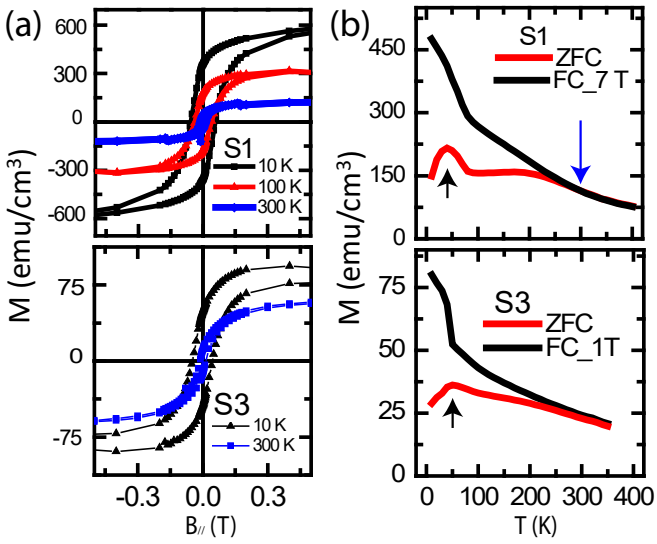

Figure 5.5: Temperature dependence of magnetic hysteresis loops of (a) sample S1 : SMO (2 nm) / STO (top panel), sample S3: SMO (17 nm)/STO (bottom panel), (b) Temperature dependent magnetization plots of S1 and S3. The black arrows 40 K indicate the magnetic phase transitions due to secondary phases and the blue arrow indicate the bifurcation of the ZFC and FC curves at 300 K indicating the magnetic phase transition of SMO film in sample S1.

M_S = 400 , 100 emu/cm^3 at 10 K and 300 K respectively are derived from M vs H plots for S1. Ferromagnetic behavior in S1 is facilitated by double exchange mechanism due to the formation of oxygen vacancies, induced by the tensile strained substrate [20, 21]. On the other hand, ferromagnetic contribution is suppressed in S3 films (bottom panel of Fig. 5.5a) as manifested in the lower values of M_S of 100, 50 emu/cm^3 at 10 and 300 K respectively. Moreover the magnetization does not reach saturation in S3 films as evident from the hysteresis loops and requires large applied fields and low temperatures, indicating the coexistence of competing magnetic interactions. Besides, S1 and S3 exhibit distinct magnetic phase transitions (T_N = 290 K for S1, T_N > 350 K for S3), as shown from the bifurcation points of zero field cooled (ZFC) and field cooled (FC) curves in Fig. 5.5(b) (dotted symbol). Furthermore, the Magnetization vs Temperature (M-T) plots show an additional antiferromagnetic phase transition at 40 K for both S1 and S3 as seen from the peak in the ZFC curves.
From the M-T plots in Fig. 5.5(b), the bifurcation in the ZFC and FC curve indicates a field dependent magnetization response and is consistent with the M vs H loops shown in Fig. 5.5(a). This observation suggest a canted antiferromagnetic phase with a weak anisotropy and/or a strong competition between coexisting double exchange FM and superexchange AFM phases across the SMO thin films. The cusp like feature around 40 K observed in the M-T plots in Fig. 5.5(b) indicates a phase transition of such a canted AFM phase to a more G-type AFM ordering intrinsic to SMO films. In order to gain an insight into the spatial extent and nature of the magnetic ordering, we have used spin Hall effect based spin transport studies as discussed in the next sections.

5.6 Transport measurements by detection of AC signals

In this chapter, the spin transport measurements were carried out by the injection and detection of AC signals using low frequency Lock-in amplifier. Using the lock-in detection technique, the first, second and higher harmon-

ics of the AC signals can be separated. In this work, we have focused on the first and second harmonic responses. This can be understood in the following way, any voltage response can be expressed as a sum of the higher harmonics as follows :

$$V(t) = R_1 I(t) + R_2 I^2(t) + R_3 I^3(t) + R_4 I^4(t) + ... \tag{5.1}$$

where R_n is the n-th order harmonic response to an applied current I(t). An AC current, $I(t) = \sqrt{2} I_o \sin(\omega t)$, is applied where ω is the angular frequency and I_0 is the rms value. The detected harmonic signals of the lock-in amplifier at a set phase of ϕ is defined as the integration over the time space T,

$$V_n(t) = \frac{\sqrt{2}}{T} \int_{t-T}^{t} sin(n\omega s + \phi) V_{in}(s) ds \tag{5.2}$$

For a given value of V_{in}, the different harmonic voltages V_n (t) can be obtained. The following harmonic responses are as follows :

$$V_1 = R_1 I_0 + \frac{3}{2} R_3 I_o^3 \text{ for } \phi = 0^o \tag{5.3}$$

$$V_2 = \frac{1}{\sqrt{2}} (R_2 I_0^2 + 2 R_4 I_0^4) \text{ for } \phi = -90^o \tag{5.4}$$

$$V_3 = -\frac{1}{2} R_3 I_0^3 \text{ for } \phi = 0^o \tag{5.5}$$

$$V_4 = -\frac{1}{2\sqrt{2}} R_4 I_0^4 \text{ for } \phi = -90^o \tag{5.6}$$

5.7 Electrical transport measurements at interface of Pt/$SrMnO_3$

UV-lithography followed by electron beam evaporation were used to pattern and fabricate the 7 nm thick-Pt based Hall bar devices (dimensions:

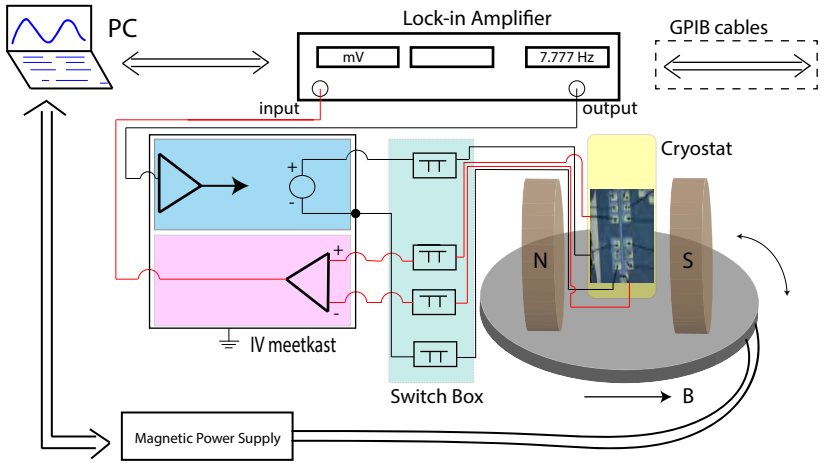

Figure 5.6: Schematic illustration of the measurement set up.

width w = 50 μm, length l = 3000 μm) on SMO thin films as shown in Fig. 5.7. Ti (t = 5 nm) and Au (t = 25 nm) contact pads were evaporated thereafter. Angle dependent spin Hall magnetoresistance (SMR) and Spin Seebeck effect (SSE) measurements were performed on a physical property measurement (PPMS) system (Quantum Design) with fields ramping up to 7 T and temperature range between 5-300 K. For field-dependent SMR and SSE measurements, a sinusoidal alternating current of amplitude I_0= 1 mA (J_0 = 2.8 x 10^9 A/m^2) and frequency (ω) = 7.77 Hz was driven across the Pt Hall bar in the y-direction. This induces Joule heating, generating an out-of-plane thermal gradient in the magnetic-SMO layer. The thermal gradient can be varied by changing the current (J_{ac}) applied across the Pt Hall bar. The current applied along the y-direction, leading to a spin accumulation (μ) pointing along the x-direction. The voltage response due to SMR and SSE effects were measured in longitudinal (V_{yy}) and transverse (V_{xy}) configurations at 7 T magnetic field. Four Lock-in amplifiers were simultaneously used to measure the first harmonic($V_{yy}^{1\omega}$ and $V_{xy}^{1\omega}$ at phase = 0^o) and second harmonic ($V_{yy}^{2\omega}$ and $V_{xy}^{2\omega}$ at phase = -90^o) voltages with a

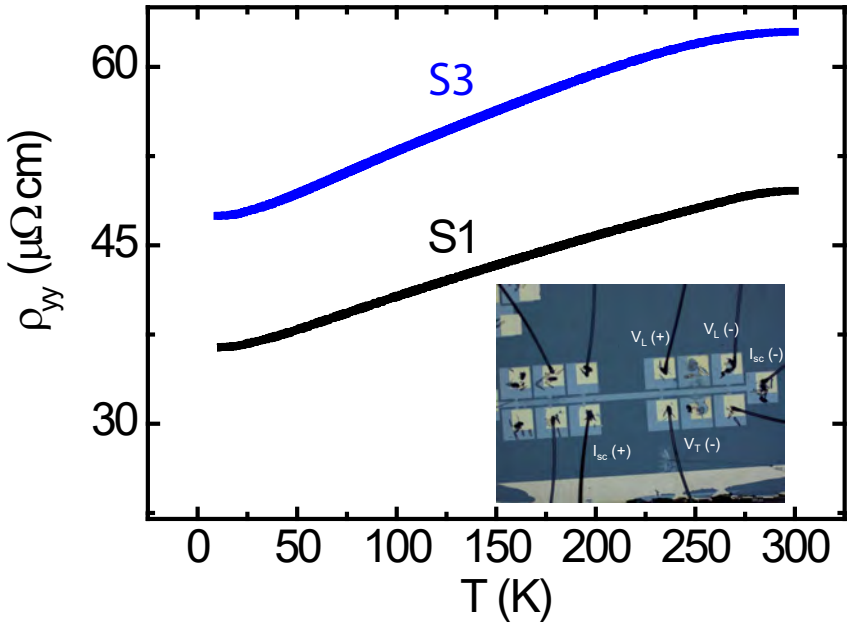

Figure 5.7: (a) The longitudinal resistivity measured for sample S1 and S3 with an applied current bias $I_0 = 1$ mA. The inset shows the optical image of the Pt Hall bar for sample S1, similar channel length and transverse contacts are also chosen for the Hall bar in sample S3. The conductivity $\sigma = 1/\rho$, where the conductivity at 10 K is around 0.027 $\mu\Omega^{-1}\text{cm}^{-1}$ for sample S1 and 0.021 $\mu\Omega^{-1}\text{cm}^{-1}$ for sample S3. Hence, the Pt resistivity lies within the intrinsic limit of its metallicity.

time constant of 3 secs by rotating the sample in the x-y (α), x-z (β) and y-z (γ) planes respectively. Spin Hall magnetoresistance (SMR) and spin Seebeck (SSE) measurements were simultaneously performed in order to study the magnetic ordering of the SMO films with different thickness from the surface and bulk magnetic contributions respectively. The schematic illustration of the electrical measurement set up is shown in Fig. 5.6.
The resistivity (ρ) variation of Pt (7 nm) with temperature for both the samples S1 and S3 are shown in Fig.5.7. Both the resistivity and the conductivity ($\sigma = 1/\rho$) of the Pt layer lies in the intrinsic limit of its metallicity

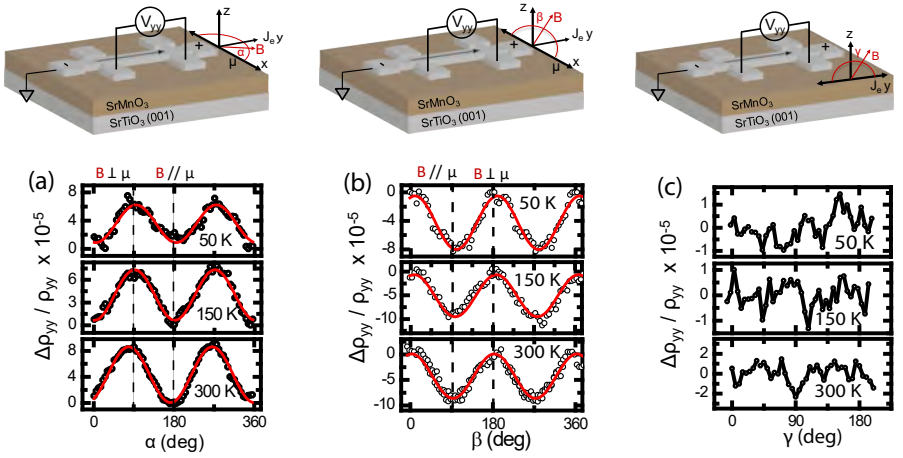

Figure 5.8: Angular dependent spin Hall magnetoresistance (AD-SMR) signals shown for three representative temperatures obtained by sweeping an applied magnetic field (B) of 7 T along (a) α, (b) β and (c) γ rotation planes for sample S1. Here J_e, μ represents the corresponding electron flow and spin accumulation directions respectively.

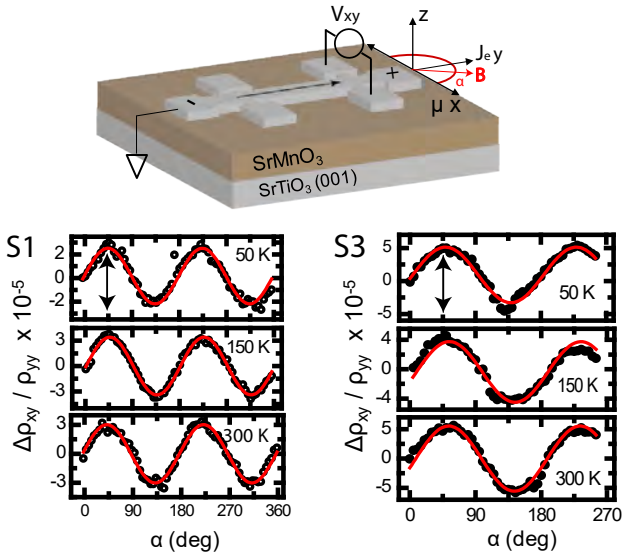

Figure 5.9: The angular dependent transverse spin Hall magnetoresistance (AD-SMR) signals shown for three representative temperatures obtained by sweeping an applied magnetic field (B) = 7 T along α rotation plane for both S1 and S3 samples. Here J_e, μ represents the corresponding electron flow and spin accumulation directions respectively

[30]. The differences in the resistivity for the two samples can be due to the differences in the interface roughness across Pt/SMO.

Figure 5.8 shows the angular dependent spin Hall magnetoresistance (AD-SMR) signals for three representative temperatures with an applied field (B) = 7 T along (a) α, (b) β, and (c) γ rotation planes for sample S1. For SMR measurements, the charge current (I) was applied along the y-direction (J_e), which creates a spin accumulation (μ) along x-direction and spin current (J_s) pointing in the -z direction due to spin Hall effect (SHE). The spin current (J_s) induced in the Pt layer exerts a torque on the magnetization (M) vector of the underlying SMO layer. Depending on the relative orientation of M and μ, reflection or absorption of spin current occurs at

the Pt/FM interface which in turn causes the modulation of spin dependent magnetoresistance.

5.8 Spin Hall Magnetoresistance across $Pt/SrMnO_3$

The typical longitudinal and transverse SMR contributions arising at the interface of Pt/SMO are given as follows[31, 32]:

$$\frac{\Delta R_{yy}}{R_o} = \frac{\Delta \rho_{yy}}{\rho_o} < 1 - m_x^2 > \propto \cos^2(\alpha, \beta) \tag{5.7}$$

$$\frac{\Delta R_{xy}}{R_o} = \frac{\Delta \rho_{xy}}{\rho_o} \frac{w}{l} < m_x m_y > \propto \sin(2\alpha) \tag{5.8}$$

where ΔR_{yy} and ΔR_{xy} are the change in the AD-SMR response measured in the longitudinal and transverse configurations respectively. $\Delta R_{yy} = R_{yy}(\alpha = 90^o)$ - $R_{yy}(\alpha = 0) = \rho_{yy}(\alpha = 90^o)$ - $\rho_{yy}(\alpha = 0)$. Here m_x, m_y and m_z refer to the projection of the magnetization along the three orthogonal axes. w, l are width and length of the Pt Hall bar and ρ_0 is the Drude resistivity. The longitudinal and transverse SMR variations shown for S1 and S2 samples (Figs. 5.8, 5.9) under 7 T field, follows a $\cos^2\alpha$ and $\sin(2\alpha)$ variation thus, consistent with 5.7 and 5.8. For the longitudinal SMR configuration shown for sample S1 in Fig. 5.8, the spin resistance displays a maximum (absorbed) and minimum (reflected) at $\alpha = 90^o$ and $\alpha = 0^o$ ($B \perp J_e$) configurations respectively, similar to SMR signals observed on Pt/YIG and other ferrimagnetic spinel systems which is commonly attributed to positive SMR [7, 8, 32] and usually occurs when the applied magnetic field exceeds the anisotropic fields in Pt/FM heterostructures as shown in Fig. 5.8. The transverse SMR for both the samples S1 and S3 shows similar variation in Fig. 5.9, with peaks at 45^o and 135^o for both the films, hence showing a $\sin(2\alpha)$ behavior as shown in Eq. 5.8. Moreover, from the amplitudes of the signals as shown by the double-headed arrow in Fig. 5.9 (a and b), a weak temperature dependence of the SMR signals are observed that will be further discussed in the next sections.

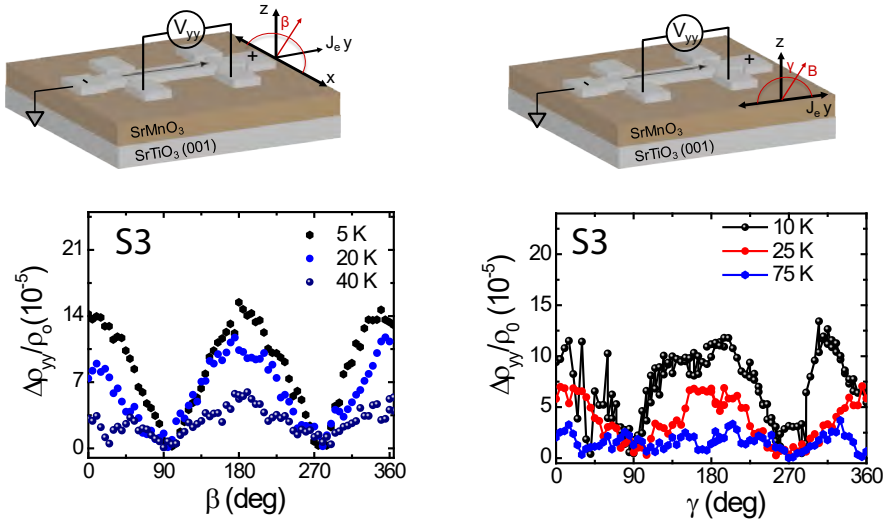

Figure 5.10: (a) The temperature dependent ADMR measurements in the x-z plane (β-direction) for sample S3 measured at a magnetic field of 7 T and current bias of I_0 = 1 mA. (b) Temperature dependent ADMR measurements in the y-z plane (γ -direction) for sample S3 at a magnetic field of 7 T and current bias of I_0 = 1 mA.

In order to confirm that the observed magnetoresistance response is from SMR and to exclude the possibility of a magnetic proximity induced AMR effect in Pt, AD-SMR measurements were also performed in the out-of-plane (oop) configuration. As shown in the Fig. 5.8(b,c), for SMR measurements in sample S1 along x-z plane, a relative change in the angle between the B field and μ occurs leading to a $\cos^2\beta$ behavior. Similar ADMR signals are also observed for sample S3 in the longitudinal contacts as shown in Fig. 5.10. However, in Fig. 5.8 (c), when the magnetic field is applied along the y-z plane, no signatures of SMR signal are observed, indicating a perpendicular alignment of the magnetic field with μ at all angles thus consistent with SMR theory and thereby excluding the proximity induced AMR effect in Pt, as reported earlier for Pt/FM hybrid systems[33, 34].

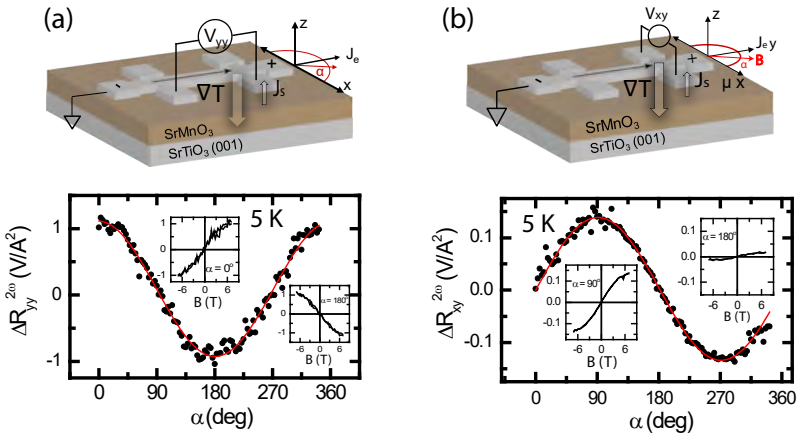

Figure 5.11: (a and b) Angular dependent SSE signals measured in the longitudinal and transverse SSE configurations at 5K by sweeping in-plane 7 T field (α scan) at a current bias of $I_0 = 1.2$ mA for sample S3. The insets shows the field dependent SSE signals acquired at dissimilar angles.

ADMR data of sample S3 are shown in Fig. 5.10, along out-of-plane (OOP) directions i.e. β, γ directions respectively measured at 7 T field for selected temperatures. It is known from literature that the ADMR signals in the oop scans can have its origins from both, (i) SMR / AMR / Hanle Magnetoresistance signals[35], (ii) anti-weak localization (which is an intrinsic effect of the platinum prominent only at low temperatures below 50 K, thereby independent of the underlying magnetic material) [35, 36]. In this regard thus observed $\cos^2\theta$ angular variation (Fig. S4) in the β and γ scans with similar amplitude values, may point towards the emergence of weak anti-localization (WAL) effect in Pt due to high spin-orbit interaction. However, for the rotation in the plane, no variation of R_{yy} data for S3 was observed due to its larger Pt/SMO interface roughness which can also inferred from the higher Pt Drude resistivity compared to S1(Fig. 5.7).

5.9 Spin Seebeck Effect (SSE)

In order to understand about the bulk magnetic properties in the thin films of S1 and S3, Spin Seebeck (SSE) measurements were performed. In Figs. 5.11 (a and b), the Spin Seebeck responses are detected in the longitudinal and transverse configurations respectively at 5 K by sweeping the in-plane 7 T field (α -scan) for sample S3. An applied current bias ($I_0 = 1.5$ mA in this case) induces a thermal gradient (∇T) creating a magnon spin accumulation (μ_m) in the bulk SMO layer, which in turn diffuses a spin current (I_s) in the Pt layer, that is detected as charge resistance due to inverse spin Hall effect (ISHE)[37, 38]. From Fig. 5.11 (a and b), a sinusoidal variation of the SSE responses are observed. The SSE signals shows a peak at 0^o and 180^o for the longitudinal contacts of Pt (Fig. 5.11a), when the applied magnetic field is parallel to the magnon spin accumulation, leading to a detectable charge resistance in Pt due to ISHE. This kind of a magnetoresistance is extracted from the 2nd harmonic response in the lockin amplifiers. These obtained signals scale quadratically with current bias indicating a thermal related spin response and a current induced phenomenon. Similar angular dependences in the SSE responses are obtained for sample S1, as discussed in the following subsections.

5.9.1 Angular dependent SSE responses

The inverse spin Hall voltage (V_{ISHE}), measured as the 2^{nd} harmonic response (2ω), in the lock-in amplifier is proportional to the magnon spin polarization (σ_m) in the insulating layer and thereby proportional to the spin polarization in Pt (σ), and related to the V_{ISHE} by[10, 37–40] :

$$V_{ISHE} \propto \theta_{SHE}(J_s \times \sigma) \tag{5.9}$$

The SSE signal as V_{ISHE} yields a maximum response for the condition when, σ is parallel to M(B), where M is the magnetization of the underlying magnetic insulator and B is the magnetic field. θ_{SHE} is the spin Hall angle of Pt and J_s is the spin current that is normal to the interface and is parallel to the temperature gradient ∇T in case of Longitudinal Spin Seebeck

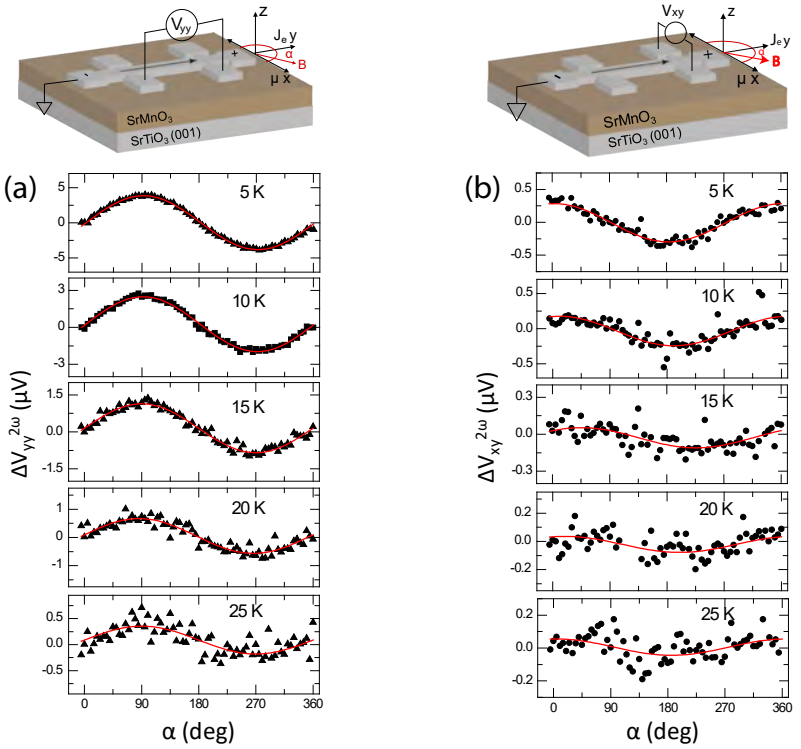

Figure 5.12: (a) Temperature dependent SSE signals due to the angular rotation is observed for sample S1. By applying a current bias of $I_0 = 1.2$ mA and applied magnetic field of 7 T in the x-y plane (α - scan). The signals are observed across the longitudinal contacts. Detectable signals are observed till 40 K above which we do not see any SSE signals. (b) Simultaneous SSE signals observed across the transverse contacts. The solid red lines in Fig. (a) and (b) are the sinusoidal fits to the SSE signals.

configuration. The extracted V_{ISHE} is proportional to square of the current bias due to Joule heating. This is shown here for sample S1, where the angular dependent signals and the quadratic dependence of the extracted maximum signals by sinusoidal fitting is shown in Fig. 5.12 and 5.13 re-

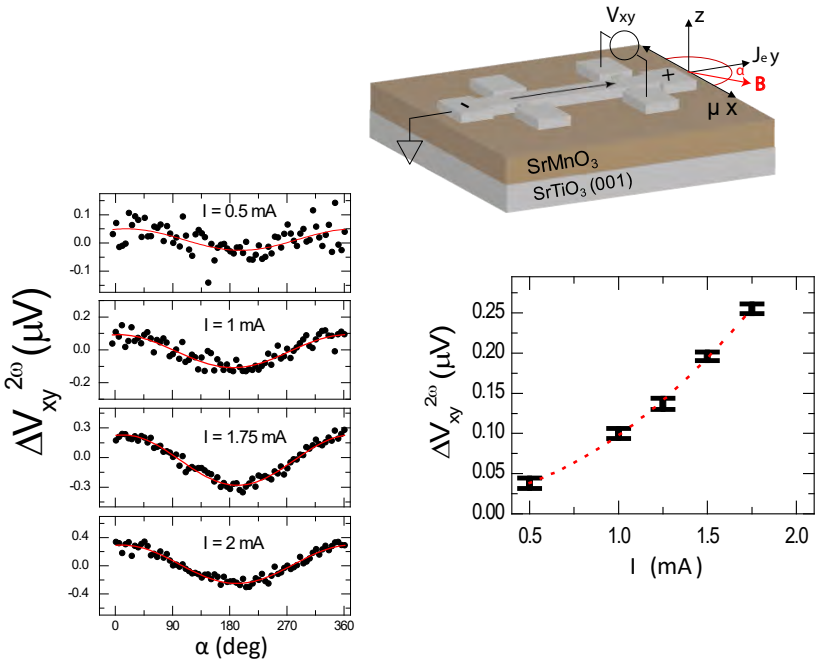

Figure 5.13: SSE signals observed in the transverse contact by applying different current bias and with an applied field of 7 T at 10 K for sample S1. The right bottom panel shows the bias dependence of the SSE voltages that are extracted from the amplitudes of the SSE signals. The red dashed line indicates a quadratic fit to the signals indicating the signals originating from the thermal effect.

spectively. Both for SMR and SSE, the measurements in the out-of-plane configuration is essential to determine the above mentioned dependence of magnetic field and spin polarization. In the out-of-plane measurement geometry, when the magnetic field is perpendicular to spin polarization (σ) at all angles, no SSE signal is expected. This is shown in Fig. 5.14, where in the γ- scan, no signals are detected by applying a magnetic field. For the β-scan however, a sinusoidal response for both the samples S1 and S3 is seen (Fig. 5.14 and 5.15), suggesting the observed signals to originate

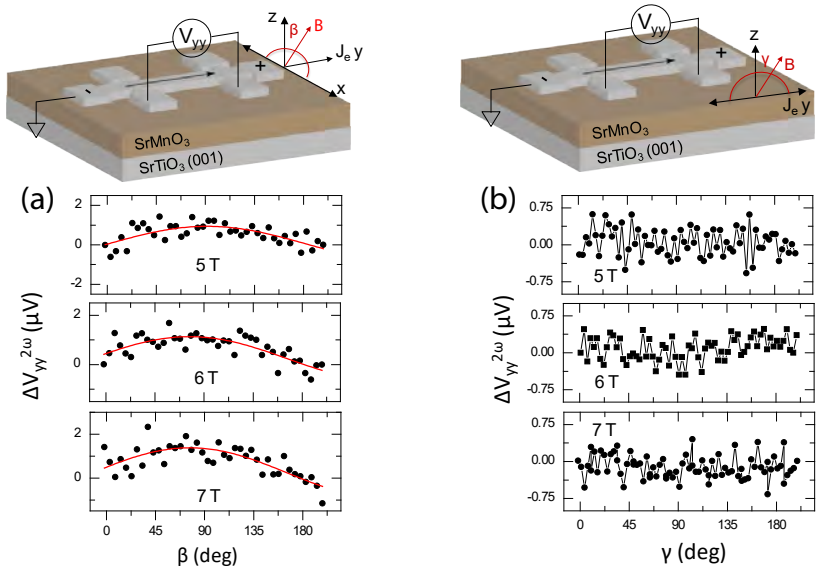

Figure 5.14: SSE signals in sample S1, observed with the angular rotation where the magnetic field B = 7 T , 6 T and 5 T, are applied in the out-of-plane configuration at 10 K, (a) x-z plane (β-scan) and (b) y-z plane (γ-scan). In the β- scan, a peak is observed around 90^o, indicating the magnetic field to be parallel to x-direction, i.e. the spin polarization (σ) in Pt. Whereas in the γ-scan, no response is observed as the magnetic field is always perpendicular to the σ, indicating the observed response in the β-scan to originate from the relative alignment of the magnetic field (magnetization) and the spin polarization, i.e. due to Spin Seebeck effect. All the measurements are performed by applying a current bias of 1 mA.

from the parallel orientation of σ and B, i.e Spin Seebeck Effect. The thermal contribution due to Anomalous Nernst effect (ANE)[41, 42], were not observed, as ANE depends on the relative orientation of the current and magnetization direction, i.e. it should be visible in the γ- scan unlike SSE.

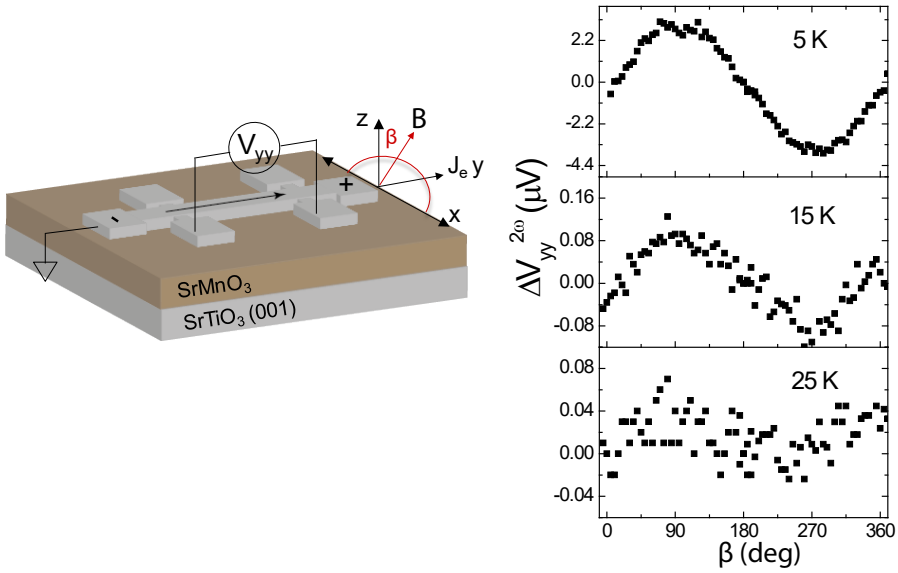

Figure 5.15: Temperature dependent SSE signals observed in the angular scan in the x-z plane (β-scan) with an applied current bias of 1 mA for sample S3. The signals are measured with an applied field of 7 T. The sinusoidal signals peak at 90^o indicating the parallel alignment of magnetic field B with the spin polarisation (σ) in the x-direction (in-plane).

5.9.2 Field dependent SSE responses

A field dependent measurements were performed at in-plane orientations where the SSE responses were maximum as shown from the angular measurements. This is shown in the inset to Fig. 5.11 (a,b) for both longitudinal and transverse configurations for sample S3. The field dependent SSE measurements displays a non-linear dependence, attributed to either a weak-ferromagnetic behavior[43] or from an easy-plane antiferromagnetic behavior[12, 40] as inferred from the absence of any hysteretic behavior with respect to the trace and retrace of the magnetic field as observed in other ferri/ferromagnetic materials [44, 45] reported in recent years. A tempera-

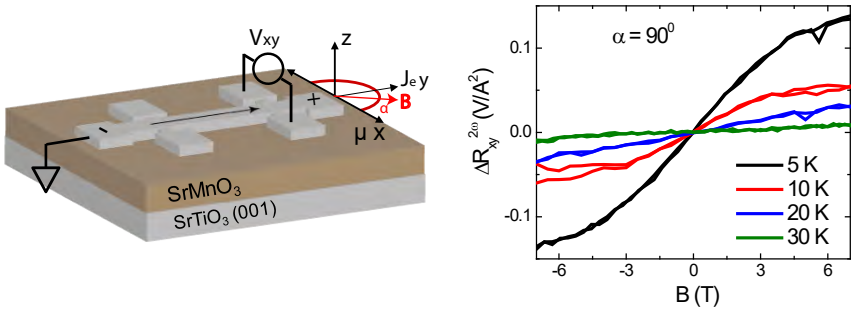

Figure 5.16: Field dependent SSE measurements performed in sample S3 at different temperatures. The measurements are shown for transverse configuration at angle $\alpha = 90^o$, where the SSE signal is maximum as shown in Fig. 5b in the main text. A linear dependence of the SSE signals are observed with increasing field dependence, resulting from the gradual response of the antiferromagnetic sublattices as the field is applied in the easy-plane direction in the SMO films.

ture dependent SSE signals are shown in Fig. 5.16 for sample S3 measured across the transverse contacts. A monotonous nonlinear response with field that vanishes after 30 K, and absence of any magnetic hysteresis indicates a field dependent response of the antiferromagnetic sublattices in the SMO films as the magnetic field that is applied in the easy-plane direction[12]. This is in contrast to the behavior shown by uniaxial AFMs that shows a spin flop transition with the applied field along the easy axis direction as shown for MnF_2 and Cr_2O_3[11, 40].

5.10 Discussion

We now discuss our findings, in the light of the different probing techniques used in this work, to establish the role of the competing and coexisting magnetic domains in the tensile strained S1 and S3 films with temperature. The SMR response, that fingerprints the surface magnetization in Pt/FMI hybrid systems[9, 35] can be identified with a ferromagnetic ordering due to a positive SMR response[32, 46] and an existence of an effective mag-

netization rather than Neel ordering[4, 32] as shown in Figs. 5.8 and 5.9 from the ADMR signals. However, this is unlike the response observed in the bulk magnetization studies as shown in Fig. 5.7(b). To reconcile this, we now take into account the temperature dependent SMR (top panel) and SSE (bottom panel) amplitudes for samples S1 and S3 at an applied magnetic field of 7 T in-plane, as shown in Fig. 5.17(a). S1 shows a temperature dependence atypical of SMR response in Pt/YIG hybrid systems [47, 48], the variation of S3 is quite unique. It saturates beyond a critical temperature, T_{crit}, but for $T < T_{crit}$, a steep decrease is observed. This temperature range corresponds to the temperature at which the ZFC curves, in Fig 5.5(b), exhibit a cusp in SQUID studies, and is ascribed to the presence of antiferromagnetic ordering in the bulk. As discussed earlier, our tensile strained films will exhibit ferromagnetic ordering, evinced in the M-H loops in Fig. 5.5(a) due to a possible $SrMnO_{3-\delta}$ phase (growth at a very low oxygen pressure) and as found in Fig. 5.17 for S1. However, to understand the temperature variation of the SMR response in S3, we recall that the additional annealing step induces competing magnetically ordered surface states that is probed by the surface sensitivity of the SMR technique. We can consider the thin film to comprise of a surface (S-SMO) and bulk (B-SMO) layer (Fig. 5.17c) and propose the presence of an AFM ordering that mimics an exchange coupling and is controlled by temperature. Thus, below $T < T_{crit}$, the enhanced strength of the exchange coupling induced ordering of the magnetic domains near the surface leads to a steep reduction in the SMR response similar to that observed in Pt/YIG hybrids with surface treatment in YIG[35] or by insertion of antiferromagnetic NiO layer[49]. Above $T>T_{crit}$, due to the reduction in the strength of the exchange, long range order restores the dominant surface ferromagnetic ordering. The idea of the spatial extent of the different magnetic ordering in SMO films classified into surface and bulk layers is not ad hoc, as earlier reports do indicate the formation of mixed phases in SMO films due to competing double exchange and superexchange interactions extending vertically, along the growth direction of the SMO films[20, 50].

From the findings of the SSE studies, we now discuss the spatial extent of the magnetic ordering across the thickness of both the samples. Unlike

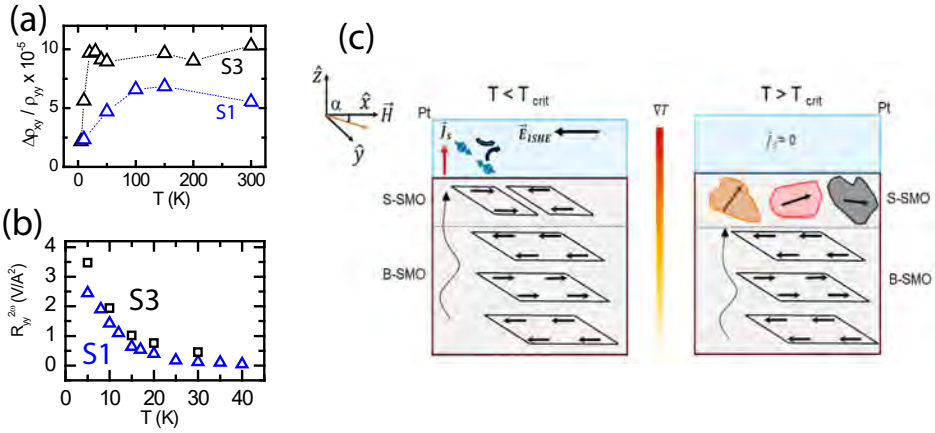

Figure 5.17: Temperature dependence of SMR (top panel) and SSE (bottom panel) signals at current bias of I_0 = 1 mA and 1.5 mA respectively and at an applied magnetic field of 7 T. The schematic at the right hand side, shows the field dependent exchange coupled ordering of the magnetic moments in the surface (S-SMO) and bulk (B-SMO) layers of the SMO films for the temperature ranges, T<T_{crit} and T>T_{crit}.

the temperature dependence of the SMR response, the SSE signal (Fig 5.17 b) shows a monotonous decrease with increasing temperature and vanishes beyond 40 K, which is close to T_{crit} (defined for SMR signals) as well as close to the temperature at which the ZFC shows a cusp (Fig. 5.7b) for both the samples S1 and S3. The temperature dependence of SSE signals depicts the role of the exchange coupled magnetic ordering, akin to an AFM order whose magnetic moments in the sublattices responds gradually with increasing applied field strength as observed from the field dependent SSE signals in Fig. 5.11 (inset) and 5.16. As shown in Fig 5.17(c), below $T < T_{crit}$, the enhanced exchange coupling strength across the S-SMO layer, induces a net AFM ordering, at a high field of 7 T, across the entire thickness, facilitating magnon excitation and propagation due to the thermal gradient that in turn diffuses a finite spin current into Pt electrodes. However for $T > T_{crit}$, the AFM long range order is weakened in between the S-and B-SMO layers hindering efficient magnon spin transport and consequently leads to the vanishing of SSE signal at higher temperatures. This suggests a coexistence of competing magnetic ordering across the SMO films. Overall, our findings reiterate the requirement of a predominant magnetic ordering at the surface of the magnetic films for magnon assisted spin transport in SSE studies[51] and the surface sensitivity of the SMR response to detect any competing magnetic ordering in such tensile strained manganite thin films. Further, SSE responses at lower temperature reported earlier in Pt/YIG[39], Pt/Cr_2O_3[40] hybrids, indicate the role of the magnon-phonon interaction due to the thermal induced phonon drag. Infrared and Raman studies have shown strong spin-phonon coupling at low temperatures (below T_N) in bulk SMO[52]. Further, first principle calculations show the strong role of spin-phonon coupling and strain in stabilizing different magnetic ordered states in $SrMnO_3$ [23, 53]. In our case, the exchange coupling at low temperatures, evident from the M-T and SSE measurements hints at magnon-phonon interaction as a possible candidate for the decrease of SSE signals with increasing temperature. However, further studies are needed to establish this. Moreover, our work necessitates the role of long range magnetic ordering for the observation of SSE signals in manganite systems, which is different from the recent reports on the observation of SSE in

paramagnets[12, 54].
Furthermore, to get insights on the Pt/SMO interface quality, we have also estimated the real part of the spin mixing conductance (G_r) as follows:

$$\frac{\Delta\rho_{xy}}{\rho_o} = \theta_{SH}^2 \frac{\lambda}{d_n} Re\left(\frac{2\lambda G_r \tanh^2(\frac{d_n}{2\lambda})}{\sigma_e + 2\lambda G_r \coth(\frac{d_n}{\lambda})}\right) \tag{5.10}$$

where (d_N) is Pt thickness, σ_e is the electrical conductivity ($\sigma = 1/\rho_o$), θ_{SH} is the spin Hall angle and λ the spin diffusion length. We estimated the spin mixing conductance (G_r) to be $\sim 10^{14}$ $\Omega^{-1}m^{-2}$ at 50 K (at 7 T field) by assuming spin Hall angle of 0.06 [7] and spin diffusion length (λ) of 3 nm [6, 55]. Thus, the estimated G_r values are around the same order reported earlier for Pt/YIG systems[7, 48], and are 3 orders of magnitude lower than the earlier report on Pt/SMO[46]. This order variation can arise due to the differences in the deposition techniques of Pt layer (evaporation in our case) and also calculation of Gr at maximum applied magnetic fields (7 T in our case) compared to the earlier report on Pt/SMO (sputtering technique, maximum applied field $\sim$ 9 T).

5.11 Summary

Our work represents a comprehensive temperature and field dependent study of magnetic ordering in SMO thin films utilizing complementary transport probes that reveals competing magnetic exchange-like behavior. Further, our study also highlights the predominant contribution of the surface magnetic layer from the temperature dependence of the SMR and SSE studies, promoted by a spatially varying strain across the films and the choice of growth parameters. This work is a first attempt to understand the complex magnetic structure in manganite insulating thin films utilizing spin transport. The ability to tune the magnetic ordering with strain and oxygen vacancies in thin films of $SrMnO_3$ is an important step towards using such materials to investigate magnon spin transport and their control by electric field in such multiferroics.

Bibliography

[1] T. Jungwirth, X. Marti, P. Wadley, and J. Wunderlich, "Antiferromagnetic spintronics," *Nature Nanotechnology* **11**(3), pp. 231–241, 2016.

[2] P. Wadley, B. Howells, J. Železný, C. Andrews, V. Hills, R. P. Campion, V. Novák, K. Olejník, F. Maccherozzi, S. S. Dhesi, S. Y. Martin, T. Wagner, J. Wunderlich, F. Freimuth, Y. Mokrousov, J. Kuneš, J. S. Chauhan, M. J. Grzybowski, A. W. Rushforth, K. Edmond, B. L. Gallagher, and T. Jungwirth, "Spintronics: Electrical switching of an antiferromagnet," *Science* **351**(6273), pp. 587–590, 2016.

[3] R. Lebrun, A. Ross, S. A. Bender, A. Qaiumzadeh, L. Baldrati, J. Cramer, A. Brataas, R. A. Duine, and M. Kläui, "Tunable long-distance spin transport in a crystalline antiferromagnetic iron oxide," *Nature* **561**(7722), pp. 222–225, 2018.

[4] G. R. Hoogeboom, A. Aqeel, T. Kuschel, T. T. Palstra, and B. J. Van Wees, "Negative spin Hall magnetoresistance of Pt on the bulk easy-plane antiferromagnet NiO," *Applied Physics Letters* **111**(5), 2017.

[5] R. Lebrun, A. Ross, O. Gomonay, S. A. Bender, L. Baldrati, F. Kronast, A. Qaiumzadeh, J. Sinova, A. Brataas, R. A. Duine, and M. Kläui, "Anisotropies and magnetic phase transitions in insulating antiferromagnets determined by a Spin-Hall magnetoresistance probe," *Communications Physics* **2**(1), pp. 1–7, 2019.

[6] L. Baldrati, A. Ross, T. Niizeki, C. Schneider, R. Ramos, J. Cramer, O. Gomonay, M. Filianina, T. Savchenko, D. Heinze, A. Kleibert, E. Saitoh, J. Sinova, and M. Kläui, "Full angular dependence of the spin Hall and ordinary magnetoresistance in epitaxial antiferromagnetic NiO(001)/Pt thin films," *Physical Review B* **98**(2), pp. 1–9, 2018.

[7] N. Vlietstra, J. Shan, V. Castel, J. Ben Youssef, G. E. Bauer, and B. J. Van Wees, "Exchange magnetic field torques in YIG/Pt bilayers observed by the spin-Hall magnetoresistance," *Applied Physics Letters* **103**(3), pp. 1–5, 2013.

[8] N. Vlietstra, J. Shan, V. Castel, B. J. Van Wees, and J. Ben Youssef, "Spin-Hall magnetoresistance in platinum on yttrium iron garnet: Dependence on platinum thickness and in-plane/out-of-plane magnetization," *Physical Review B - Condensed Matter and Materials Physics* **87**(18), pp. 1–5, 2013.

[9] M. Isasa, S. Vélez, E. Sagasta, A. Bedoya-Pinto, N. Dix, F. Sánchez, L. E. Hueso, J. Fontcuberta, and F. Casanova, "Spin Hall Magnetoresistance as a Probe for Surface Magnetization in Pt/CoFe2 O4 Bilayers," *Physical Review Applied* **6**(3), pp. 1–10, 2016.

[10] A. Aqeel, N. Vlietstra, J. A. Heuver, G. E. Bauer, B. Noheda, B. J. Van Wees, and T. T. Palstra, "Spin-Hall magnetoresistance and spin Seebeck effect in spin-spiral and paramagnetic phases of multiferroic CoCr2O4 films," *Physical Review B - Condensed Matter and Materials Physics* **92**(22), pp. 1–8, 2015.

[11] S. M. Wu, W. Zhang, A. Kc, P. Borisov, J. E. Pearson, J. S. Jiang, D. Lederman, A. Hoffmann, and A. Bhattacharya, "Antiferromagnetic Spin Seebeck Effect," *Physical Review Letters* **116**(9), pp. 1–5, 2016.

[12] J. Li, Z. Shi, V. H. Ortiz, M. Aldosary, C. Chen, V. Aji, P. Wei, and J. Shi, "Spin Seebeck Effect from Antiferromagnetic Magnons and Critical Spin Fluctuations in Epitaxial FeF2 Films," *Physical Review Letters* **122**(21), p. 217204, 2019.

[13] C. Liu, S. M. Wu, J. E. Pearson, J. S. Jiang, N. D'Ambrumenil, and A. Bhattacharya, "Probing short-range magnetic order in a geometrically frustrated magnet by means of the spin Seebeck effect," *Physical Review B* **98**(6), pp. 1–6, 2018.

[14] Y. Tokura, "Critical features of colossal magnetoresistive manganites," *Reports on Progress in Physics* **69**(3), pp. 797–851, 2006.

[15] J.-P. Renard and a M Haghiri-Gosnet, "CMR manganites: physics, thin films and devices," *Journal of Physics D: Applied Physics* **36**(8), pp. R127—-R150, 2003.

[16] R. Søndenå, P. Ravindran, S. Stølen, T. Grande, and M. Hanfland, "Electronic structure and magnetic properties of cubic and hexagonal SrMn O3," *Physical Review B - Condensed Matter and Materials Physics* **74**(14), pp. 1–12, 2006.

[17] D. M. Nalecz, R. Bujakiewicz-Koronska, and R. J. Radwanski, "Magnetic phase transition in antiferromagnetic SrMnO3 perovskites," *Ferroelectrics* **483**(1), pp. 86–94, 2015.

[18] L. Maurel, N. Marcano, T. Prokscha, E. Langenberg, J. Blasco, R. Guzmán, A. Suter, C. Magén, L. Morellón, M. R. Ibarra, J. A. Pardo, and P. A. Algarabel, "Nature of antiferromagnetic order in epitaxially strained multiferroic SrMnO3 thin films," *Physical Review B - Condensed Matter and Materials Physics* **92**(2), pp. 1–9, 2015.

[19] J. H. Lee and K. M. Rabe, "Epitaxial-strain-induced multiferroicity in SrMnO3 from first principles," *Physical Review Letters* **104**(20), pp. 2–5, 2010.

[20] F. Wang, Y. Q. Zhang, Y. Bai, W. Liu, H. R. Zhang, W. Y. Wang, S. K. Li, S. Ma, X. G. Zhao, J. R. Sun, Z. H. Wang, Z. J. Wang, and Z. D. Zhang, "Oxygen vacancy formation, crystal structures, and magnetic properties of three SrMnO3-δ films," *Applied Physics Letters* **109**(5), 2016.

[21] C. Becher, L. Maurel, U. Aschauer, M. Lilienblum, C. Magén, D. Meier, E. Langenberg, M. Trassin, J. Blasco, I. P. Krug, P. A. Algarabel, N. A. Spaldin, J. A. Pardo, and M. Fiebig, "Strain-induced coupling of electrical polarization and structural defects in SrMnO 3 films," *Nature Nanotechnology* **10**(8), pp. 661–665, 2015.

[22] J. W. Guo, P. S. Wang, Y. Yuan, Q. He, J. L. Lu, T. Z. Chen, S. Z. Yang, Y. J. Wang, R. Erni, M. D. Rossell, V. Gopalan, H. J. Xiang, Y. Tokura, and P. Yu, "Strain-induced ferroelectricity and spin-lattice coupling in SrMn O3 thin films," *Physical Review B* **97**(23), pp. 1–8, 2018.

[23] A. Edström and C. Ederer, "First-principles-based strain and temperature-dependent ferroic phase diagram of SrMnO3," *Physical Review Materials* **2**(10), pp. 1–12, 2018.

[24] A. Edström and C. Ederer, " Prediction of a Giant Magnetoelectric Cross-Caloric Effect around a Tetracritical Point in Multiferroic SrMnO 3 ," *Physical Review Letters* **124**(16), p. 167201, 2020.

[25] J. F. Ding, O. I. Lebedev, S. Turner, Y. F. Tian, W. J. Hu, J. W. Seo, C. Panagopoulos, W. Prellier, G. Van Tendeloo, and T. Wu, "Interfacial spin glass state and exchange bias in manganite bilayers with competing magnetic orders," *Physical Review B - Condensed Matter and Materials Physics* **87**(5), pp. 1–7, 2013.

[26] S. Smadici, B. B. Nelson-Cheeseman, A. Bhattacharya, and P. Abbamonte, "Interface ferromagnetism in a SrMnO3/LaMnO3 superlattice," *Physical Review B - Condensed Matter and Materials Physics* **86**(17), pp. 1–9, 2012.

[27] T. Mori, K. Inoue, N. Kamegashira, Y. Yamaguchi, and K. Ohoyama, "Neutron diffraction study of Sr2Mn2O5," *Journal of Alloys and Compounds* **296**(1-2), pp. 92–97, 2000.

[28] S. Kobayashi, Y. Ikuhara, and T. Yamamoto, "Labyrinth-type domain structure of heteroepitaxial SrMnO2.5 film," *Applied Physics Letters* **102**(23), pp. 1–6, 2013.

[29] G. F. Harrington, A. Cavallaro, D. W. McComb, S. J. Skinner, and J. A. Kilner, "The effects of lattice strain, dislocations, and microstructure on the transport properties of YSZ films," *Physical Chemistry Chemical Physics* **19**(22), pp. 14319–14336, 2017.

[30] E. Sagasta, Y. Omori, M. Isasa, M. Gradhand, L. E. Hueso, Y. Niimi, Y. Otani, and F. Casanova, "Tuning the spin Hall effect of Pt from the moderately dirty to the superclean regime," *Physical Review B* **94**(6), pp. 1–6, 2016.

[31] Y. T. Chen, S. Takahashi, H. Nakayama, M. Althammer, S. T. Goennenwein, E. Saitoh, and G. E. Bauer, "Theory of spin Hall magnetoresistance," *Physical Review B - Condensed Matter and Materials Physics* **87**(14), 2013.

[32] J. Fischer, O. Gomonay, R. Schlitz, K. Ganzhorn, N. Vlietstra, M. Althammer, H. Huebl, M. Opel, R. Gross, S. T. Goennenwein, and S. Geprägs, "Spin Hall magnetoresistance in antiferromagnet/heavy-metal heterostructures," *Physical Review B* **97**(1), pp. 1–9, 2018.

[33] M. Althammer, S. Meyer, H. Nakayama, M. Schreier, S. Altmannshofer, M. Weiler, H. Huebl, S. Geprägs, M. Opel, R. Gross, D. Meier, C. Klewe, T. Kuschel, J. M. Schmalhorst, G. Reiss, L. Shen, A. Gupta, Y. T. Chen, G. E. Bauer, E. Saitoh, and S. T. Goennenwein, "Quantitative study of the spin Hall magnetoresistance in ferromagnetic insulator/normal metal hybrids," *Physical Review B - Condensed Matter and Materials Physics* **87**(22), pp. 1–15, 2013.

[34] Y. Cheng, S. Yu, A. S. Ahmed, M. Zhu, Y. Rao, M. Ghazisaeidi, J. Hwang, and F. Yang, "Anisotropic magnetoresistance and nontrivial spin Hall magnetoresistance in Pt/α- F e2 O3 bilayers," *Physical Review B* **100**(22), pp. 1–7, 2019.

[35] S. Vélez, V. N. Golovach, A. Bedoya-Pinto, M. Isasa, E. Sagasta, M. Abadia, C. Rogero, L. E. Hueso, F. S. Bergeret, and F. Casanova, "Hanle Magnetoresistance in Thin Metal Films with Strong Spin-Orbit Coupling," *Physical Review Letters* **116**(1), pp. 1–6, 2016.

[36] Y. Shiomi, T. Ohtani, S. Iguchi, T. Sasaki, Z. Qiu, H. Nakayama, K. Uchida, and E. Saitoh, "Interface-dependent magnetotransport properties for thin Pt films on ferrimagnetic Y3Fe5O12," *Applied Physics Letters* **104**(24), 2014.

[37] K. Uchida, S. Takahashi, K. Harii, J. Ieda, W. Koshibae, K. Ando, S. Maekawa, and E. Saitoh, "Observation of the spin Seebeck effect," *Nature* **455**(7214), pp. 778–781, 2008.

[38] G. E. Bauer, E. Saitoh, and B. J. Van Wees, "Spin caloritronics," *Nature Materials* **11**(5), pp. 391–399, 2012.

[39] K. Uchida, T. Ota, H. Adachi, J. Xiao, T. Nonaka, Y. Kajiwara, G. E. Bauer, S. Maekawa, and E. Saitoh, "Thermal spin pumping and magnon-phonon-mediated spin-Seebeck effect," *Journal of Applied Physics* **111**(10), 2012.

[40] S. Seki, T. Ideue, M. Kubota, Y. Kozuka, R. Takagi, M. Nakamura, Y. Kaneko, M. Kawasaki, and Y. Tokura, "Thermal Generation of Spin Current in an Antiferromagnet," *Physical Review Letters* **115**(26), pp. 1–5, 2015.

[41] T. Kikkawa, K. Uchida, S. Daimon, Y. Shiomi, H. Adachi, Z. Qiu, D. Hou, X. F. Jin, S. Maekawa, and E. Saitoh, "Separation of longitudinal spin Seebeck effect from anomalous Nernst effect: Determination of origin of transverse thermoelectric voltage in metal/insulator junctions," *Physical Review B - Condensed Matter and Materials Physics* **88**(21), 2013.

[42] R. Ramos, T. Kikkawa, A. Anadón, I. Lucas, T. Niizeki, K. Uchida, P. A. Algarabel, L. Morellón, M. H. Aguirre, M. R. Ibarra, and E. Saitoh, "Interface-induced anomalous Nernst effect in Fe3O4/Pt-based heterostructures," *Applied Physics Letters* **114**(11), 2019.

[43] D. Hong, C. Liu, J. E. Pearson, A. Hoffmann, D. D. Fong, and A. Bhattacharya, "Spin Seebeck effect in insulating SrFeO3-δ films," *Applied Physics Letters* **114**(24), 2019.

[44] N. Vlietstra, J. Shan, B. J. Van Wees, M. Isasa, F. Casanova, and J. Ben Youssef, "Simultaneous detection of the spin-Hall magnetoresistance and the spin-Seebeck effect in platinum and tantalum on yttrium iron garnet," *Physical Review B - Condensed Matter and Materials Physics* **90**(17), pp. 1–8, 2014.

[45] Y. Chen, D. Roy, E. Cogulu, H. Chang, M. Wu, and A. D. Kent, "First harmonic measurements of the spin Seebeck effect," *Applied Physics Letters* **113**(20), 2018.

[46] J. H. Han, C. Song, F. Li, Y. Y. Wang, G. Y. Wang, Q. H. Yang, and F. Pan, "Antiferromagnet-controlled spin current transport in SrMnO3/Pt hybrids," *Physical Review B - Condensed Matter and Materials Physics* **90**(14), pp. 1–5, 2014.

[47] S. Vélez, A. Bedoya-Pinto, W. Yan, L. E. Hueso, and F. Casanova, "Competing effects at Pt/YIG interfaces: Spin Hall magnetoresistance, magnon excitations, and magnetic frustration," *Physical Review B* **94**(17), pp. 1–8, 2016.

[48] S. Meyer, M. Althammer, S. Geprägs, M. Opel, R. Gross, and S. T. Goennenwein, "Temperature dependent spin transport properties of platinum inferred from spin Hall magnetoresistance measurements," *Applied Physics Letters* **104**(24), 2014.

[49] D. Hou, Z. Qiu, J. Barker, K. Sato, K. Yamamoto, S. Vélez, J. M. Gomez-Perez, L. E. Hueso, F. Casanova, and E. Saitoh, "Tunable Sign Change of Spin Hall Magnetoresistance in Pt/NiO/YIG Structures," *Physical Review Letters* **118**(14), pp. 1–6, 2017.

[50] J. Bai, J. Yang, W. Dong, Y. Zhang, W. Bai, and X. Tang, "Structural and magnetic properties of perovskite SrMnO3 thin films grown by molecular beam epitaxy," *Thin Solid Films* **644**(April), pp. 57–64, 2017.

[51] I. Gray, T. Moriyama, N. Sivadas, G. M. Stiehl, J. T. Heron, R. Need, B. J. Kirby, D. H. Low, K. C. Nowack, D. G. Schlom, D. C. Ralph, T. Ono, and G. D. Fuchs, "Spin Seebeck Imaging of Spin-Torque Switching in Antiferromagnetic Pt/NiO Heterostructures," *Physical Review X* **9**(4), p. 41016, 2019.

[52] S. Kamba, V. Goian, V. Skoromets, J. Hejtmánek, V. Bovtun, M. Kempa, F. Borodavka, P. Vaněk, A. A. Belik, J. H. Lee, O. Pacherová, and K. M. Rabe, "Strong spin-phonon coupling in infrared and Raman spectra of SrMnO 3," *Physical Review B - Condensed Matter and Materials Physics* **89**(6), pp. 1–8, 2014.

[53] X. Zhu, A. Edström, and C. Ederer, "Magnetic exchange interactions in SrMnO3," *Physical Review B* **101**(6), p. 64401, 2020.

[54] K. Oyanagi, S. Takahashi, L. J. Cornelissen, J. Shan, S. Daimon, T. Kikkawa, G. E. Bauer, B. J. van Wees, and E. Saitoh, "Spin transport in insulators without exchange stiffness," *Nature Communications* **10**(1), pp. 3–8, 2019.

[55] M. Isasa, E. Villamor, L. E. Hueso, M. Gradhand, and F. Casanova, "Temperature dependence of spin diffusion length and spin Hall angle in Au and Pt," *Physical Review B - Condensed Matter and Materials Physics* **91**(2), pp. 1–7, 2015.